Numerical simulation of 3D hypersonic flows

Marie-Claude Ciccoli

▶ **To cite this version:**

Marie-Claude Ciccoli. Numerical simulation of 3D hypersonic flows. [Research Report] RR-2201, INRIA. 1994. inria-00074470

HAL Id: inria-00074470
https://inria.hal.science/inria-00074470

Submitted on 24 May 2006

HAL is a multi-disciplinary open access archive for the deposit and dissemination of scientific research documents, whether they are published or not. The documents may come from teaching and research institutions in France or abroad, or from public or private research centers.

L'archive ouverte pluridisciplinaire **HAL**, est destinée au dépôt et à la diffusion de documents scientifiques de niveau recherche, publiés ou non, émanant des établissements d'enseignement et de recherche français ou étrangers, des laboratoires publics ou privés.

INRIA

INSTITUT NATIONAL DE RECHERCHE EN INFORMATIQUE ET AUTOMATIQUE

NUMERICAL SIMULATION OF 3D HYPERSONIC FLOWS

Marie-Claude CICCOLI

N° 2201

Février 1994

PROGRAMME 6

Calcul scientifique,

modélisation

et logiciel numérique

ISSN 0249-6399

INRIA
SOPHIA ANTIPOLIS

NUMERICAL SIMULATION OF 3D HYPERSONIC FLOWS

Marie-Claude CICCOLI

Programme 6 — Calcul scientifique, modélisation et logiciel numérique
Projet Sinus

Rapport de recherche n ° 2201 — Février 1994 — 38 pages

Abstract: Our objective is to develop an efficient code for 3D inviscid chemical non-equilibrium flows. Such flows are modeled by the Euler equations and by the chemical species balance equations. We present the time implicit scheme for the species equations constructed with two different sets of jacobian matrices. We also extend this implicit scheme to second-order spatial approximation. Then we compare the solutions obtained by this code with theoretical and experimental solutions in the case of a sphere. Finally we compute a non-equilibrium flow around a double ellipsoid geometry which models the nose of a shuttle.

Key-words: hypersonic, chemical non-equilibrium, implicit scheme

(Résumé : tsvp)

Unité de recherche INRIA Sophia-Antipolis
2004 route des Lucioles, BP 93, 06902 SOPHIA-ANTIPOLIS Cedex (France)
Téléphone : (33) 93 65 77 77 – Télécopie : (33) 93 65 77 65

SIMULATION NUMERIQUE D'ECOULEMENTS HYPERSONIQUES TRIDIMENSIONNELS

Résumé : Notre but est de développer un code de calcul efficace pour des écoulements hors-équilibre chimique tridimensionnels. De tels écoulements sont modélisés par les équations d'Euler et par les équations des espèces chimiques. Nous présentons le schéma en temps implicite pour les équations de la chimie construit avec deux ensembles de matrices jacobiennes différentes. Nous étendons le schéma implicite à l'ordre deux en espace. Puis nous comparons les solutions obtenues par ce code aux solutions théoriques et expérimentales pour le cas d'une sphère. Enfin nous calculons un écoulement hors-équilibre autour d'une géométrie de double ellipsoïde modélisant le nez d'une navette.

Mots-clé : hypersonique, hors-équilibre chimique, schéma implicite

Contents

1 INTRODUCTION

In the past few years, important efforts have been devoted to research on numerical methodologies for the prediction and validation of hypersonic flows [1], [9].

For a typical point of the trajectory of a reentry vehicle (Mach number 25, altitude 75 km), it is clear that a shock layer is far from chemical equilibrium [2]. Thus, equilibrium-flow solvers, sufficient to compute pressure fields, are inadequate for a detailed analysis of chemical reacting flows.

Note that other forms of non-equilibrium effects, such as thermal non-equilibrium, are also usually present in such flows. It is assumed here that these effects which are usually significant in only small regions of the flowfield can be neglected, whereas their inclusion would yield prohibitive computational work. Also, in view of possibly large 3D computations, the present approach is limited to inviscid flows governed by the Euler equations.

Thus, the objective here has been to develop an efficient code for 3D steady inviscid chemical non-equilibrium flows.

In a first step, we construct a time implicit scheme with two different sets of Jacobian matrices for the chemistry equations. We also extend this implicit scheme to second-order spatial approximation. Then we compare the solutions obtained by this code with theoretical and experimental solutions in the case of a sphere. And finally we compute a non-equilibrium flow around a double ellipsoid geometry which models the nose of a shuttle.

2 GOVERNING EQUATIONS

The set of governing equations is made of the Euler equations written in conservation-law form and Cartesian coordinates :

$$W_t + F_x(W) + G_y(W) + H_z(W) = 0 \tag{1}$$

in which

$$W = \begin{pmatrix} \rho \\ \rho u \\ \rho v \\ \rho w \\ E \end{pmatrix}$$

$$F(W) = \begin{pmatrix} \rho u \\ \rho u^2 + p \\ \rho uv \\ \rho uw \\ u(E+p) \end{pmatrix} \quad G(W) = \begin{pmatrix} \rho v \\ \rho uv \\ \rho v^2 + p \\ \rho vw \\ v(E+p) \end{pmatrix} \quad H(W) = \begin{pmatrix} \rho w \\ \rho uw \\ \rho vw \\ \rho w^2 + p \\ w(E+p) \end{pmatrix}$$

where ρ is the density, $\vec{V} = (u, v, w)$ the velocity, E the total energy per unit volume.

The species are governed by the following species balance equations :

$$(\chi_s)_t + \text{div}\left(\chi_s \vec{V}\right) = \Omega_s \qquad (s = 1, ..., N_s) \tag{2}$$

Here N_s stands for the number of species considered in the non-equilibrium model, χ_s for the partial density of species s and Ω_s for the production rate of species s.

We consider, here, a 5 species model made of N_2, O_2, NO, N and O subject to the Zel'Dovich 17 reactional scheme :

$$\begin{aligned} O_2 + X &\rightleftharpoons O + O + X \\ N_2 + X &\rightleftharpoons N + N + X \\ NO + X &\rightleftharpoons N + O + X \\ NO + O &\rightleftharpoons O_2 + N \\ N_2 + O &\rightleftharpoons NO + N \end{aligned}$$

where X stands for an arbitrary species. The production rates of these reactions are given by the Park model [3].
In fact, the definition of mass fractions and the global conservation of atoms of oxygen and nitrogen allow us to solve only the balance equations for O, N and NO [5].

The pressure is calculated by the state law which, if each species is a perfect gas, has the following form :

$$p = \rho \mathcal{R} T \sum_{s=1}^{N_s} \frac{Y_s}{m_s}$$

where $\mathcal{R}$ is the perfect gas constant, T is the temperature, Y_s is the mass fraction of species s and m_s is the molar mass of species s.

The temperature is carried out by a fixed-point algorithm from the expression of the energy [5], which is a non-linear fonction of the temperature :

$$E(T) = E_c + H_0 + E_{c_v}(T) + E_{\text{vib}}(T)$$

where E_c is the kinetic energy, H_0 is the enthalpy of formation, E_{c_v} is the internal energy and E_{vib} is the vibrational energy.

In the next section, we present the essential ingredients of our numerical method to solve the Euler equations coupled with the chemistry equations.

3 NUMERICAL METHOD

We are interested in the steady solution of the system of equations (1),(2). This solution is obtained by time integration, startong from an arbitrary initial condition. This is allowed because the system is hyperbolic in time. This artifice is used because the steady system becomes elliptic in the subsonic region. In fact, the equations (1) and (2) are solved in a decoupled manner as described in [5], this reduces considerably storage requirements compared with a fully-coupled approach. The Euler variables (ρ, ρu, ρv, E) are first computed, the local chemical composition being frozen. The temperature is then updated. And finally we reevaluate the chemical variables before calculating the new temperature. The spatial approximation of the equations is constructed using a finite-volume/finite-element discretization. For highly compressible flows, and hypersonic flows in particular, upwind finite-volume type approximation schemes present several advantages. Conservation is satisfied discretely in a trivial manner and artificial viscosity which is inherent to the approximation is controled without tuning many unphysical parameters.

3.1 Spatial Discretization

We use a tetrahedral grid from which we construct control volumes around each node. Thus a finite-volume integration of (1) related to node i leads to evaluate a flux balance for each segment ij, $j \in K(i)$ ($K(i)$ is the set of neighbors of node i), using a numerical flux function as follows :

$$\mathcal{V}_i \frac{W_i^{n+1} - W_i^n}{\Delta t} + \sum_{j \in K(i)} \Phi(W_i, W_j, \vec{\eta_{ij}}) = 0 \tag{3}$$

where $\mathcal{V}_i$ is value of the control volume around the node i and $\vec{\eta_{ij}}$ is its normal vector. To calculate the numerical fluxes for the Euler equations (1) we use a Van Leer flux vector splitting :

$$\Phi(W_i, W_j, \vec{\eta_{ij}}) = \mathcal{F}_{VL}^{+}(W_i) + \mathcal{F}_{VL}^{-}(W_j) \tag{4}$$

Accordingly, the numerical flux associated to species s is evaluated as follows :

$$\Phi_c(\chi_{si}, \chi_{sj}, \vec{\eta_{ij}}) = Y_{si}\mathcal{F}_{VL}^{1+}(W_i) + Y_{sj}\mathcal{F}_{VL}^{1-}(W_j) \tag{5}$$

where $\mathcal{F}_{VL}^{1+}$ and $\mathcal{F}_{VL}^{1-}$ are the first components of respectively the plus and minus parts ($\mathcal{F}_{VL}^{+}$ and $\mathcal{F}_{VL}^{-}$) of the Van Leer flux vector splitting. A finite-volume scheme applied to the chemistry equations (2) writes :

$$\mathcal{V}_i \frac{\chi_i^{n+1} - \chi_i^n}{\Delta t} + \sum_{j \in K(i)} \Phi_c(\chi_i, \chi_j, \vec{\eta_{ij}}) = \Omega_i \tag{6}$$

in which $\chi = (\chi_s)_{s=1,3}$ and $\Omega = (\Omega_s)_{s=1,3}$.

3.2 Time integration

In order to compute stationary solutions efficiently, an implicit temporal integration is employed. An Euler implicit scheme applied to the Euler equations (1) is obtained if the flux function Φ in (3) is evaluated at the time step $n+1$:

$$\Phi(W_i, W_j, \vec{\eta_{ij}}) = \Phi^{n+1}(W_i, W_j, \vec{\eta_{ij}}) \tag{7}$$

The fluxes are linearized [4] and the resulting scheme is written in "delta" formulation :

$$\mathcal{V}_i \frac{\delta W_i^{n+1}}{\Delta t} + \sum_{j \in K(i)} (A_{ij}\ \delta W_i^{n+1} + B_{ij}\ \delta W_j^{n+1}) = - \sum_{j \in K(i)} \Phi^n(W_i, W_j, \vec{\eta_{ij}}) \quad (8)$$

where

$$\delta W^{n+1} = W^{n+1} - W^n, \quad A_{ij} = \left[A_{ij}^{(l,m)}\right]_{l,m=1,5} \quad \text{and} \quad B_{ij} = \left[B_{ij}^{(l,m)}\right]_{l,m=1,5}$$

The matrices A_{ij} and B_{ij} we consider here are those of the Steger-Warming decomposition which leads to robust approximations according to our experience. An implicit scheme for the species balance equations is constructed in a similar way :

$$\mathcal{V}_i \frac{\delta \chi_i^{n+1}}{\Delta t} + \sum_{j \in K(i)} \left(A_{ij}^c \delta \chi_i^{n+1} + B_{ij}^c \delta \chi_j^{n+1}\right) - \frac{\partial \Omega_i}{\partial \chi_i} \delta \chi_i^{n+1} = \Omega_i - \sum_{j \in K(i)} \Phi_c^n(\chi_i, \chi_j, \vec{\eta_{ij}}) \quad (9)$$

Several choices can be made for the matrices A_{ij}^c and B_{ij}^c. All the matrices we consider here have the same following form :

$$A_{ij}^c = \frac{m_{ij}}{\rho_i}\ \mathrm{Id} \qquad \text{and} \qquad B_{ij}^c = \frac{m_{ji}}{\rho_j}\ \mathrm{Id}$$

which is this of the true Jacobian matrices of the numerical fluxes described in (5), as shown in [5]. We employ here two different sets of matrices, the true Jacobian matrices :

$$A_{ij}^c = \frac{\mathcal{F}_{VL}^{1+}(W_i)}{\rho_i}\ \mathrm{Id} \qquad \text{and} \qquad B_{ij}^c = \frac{\mathcal{F}_{VL}^{1-}(W_j)}{\rho_j}\ \mathrm{Id} \quad (10)$$

and matrices constructed to match, in some sense, the Jacobian matrices of the Euler fluxes :

$$A_{ij}^c = \frac{\sum_{m=1}^{5} A_{ij}^{(1,m)} W_i^{(m)^n}}{\rho_i^n}\ \mathrm{Id} \qquad \text{and} \qquad B_{ij}^c = \frac{\sum_{m=1}^{5} B_{ij}^{(1,m)} W_j^{(m)^n}}{\rho_j^n}\ \mathrm{Id} \quad (11)$$

We will discuss in section 4 results obtained with these two sets of matrices.

Finally, the systems (8), (9) resulting from the implicit schemes are partially solved by a few relaxation sweeps (Jacobi or Gauss-Seidel), and the update is made subsequently :

$$W^{n+1} = W^n + \delta W^{n+1} \qquad \text{and} \qquad \chi^{n+1} = \chi^n + \delta\chi^{n+1}$$

3.3 Second-order approximation

To achieve second-order spatial accuracy of the steady-state solution, the fluxes only are amended : fluxes at the interfaces are calculated in terms of MUSCL extrapolations of the physical variables as described in [6].

4 COMPUTATIONAL RESULTS

All the results we present here have been computed on a Cray YMP.

4.1 Comparison with theory

First, the accuracy of the employed finite-volume approximation is assessed. We have compared the inert-gas solution around a sphere obtained by our code, solving only the Euler equations, with the known theoretical solution of [8]. For this calculation, we employ a tetrahedral mesh of 12787 points (Figure 1) and a first-order spatial approximation. On Figure 2(a), we have plotted the distribution of the computed Mach number along the stagnation-point streamline and on Figure 2(b) the Mach-number isolines of the theoretical solution are reproduced. The computational result is to compared with the theoretical solution at Mach number equal to 10 because the stand-off distance varies very little for Mach numbers over 10 (Mach number independence principle). We can see the computational stand-off distance is found very close to the theoretical one. We also compare the computational sonic line to the theoretical sonic line on Figure 3. As expected, because of artificial viscosity, the computational subsonic pocket contains the theoretical subsonic pocket but the computational sonic line is not so far from the theoretical one. In particular the sonic point on the body is about the same. In conclusion, the finite-volume

scheme employed is accurate enough to provide us a computational solution close to the theoretical one even with a first-order spatial approximation.

4.2 Comparison with experimental results

We also want to compare our results to experimentations. We choose an experimentation performed by Vetter et al. and presented at [9]. The flow conditions for this experimentation were the following :

$$\begin{cases} T_\infty &= 196 \text{ K} \\ \rho_\infty &= 0.0016 \text{ kg/m}^3 \\ M_\infty &= 12.7 \\ Re_\infty &= 430000 \text{ /m} \end{cases}$$

T_∞, ρ_∞, M_∞ and Re_∞ are respectively the temperature, the density, the Mach number and the Reynolds number of the freestream in front of the sphere. On Figure 4 we have plotted the Cp along the body. Of course the experimental result should be compared with a viscous calculation. But the pressure distribution does not change much between an inviscid and a viscous calculation, because the pressure gradient is equal zero in the boundary layer and outside the boudary layer viscous effects can be neglected. So, an inviscid calculation is sufficient to yield an accurate pressure distribution (of course it is not true for the other variables) as is customary in Industry. We can see on Figure 4 that the Cp distribution of the computational result matches well with that of the experimental one.

4.3 Sphere calculations

In the previous calculations an inert gas model was used. Now, here a non-equilibrium gas model is employed and the freestream conditions are those of the standard atmosphere at the altitude of 75 km :

$$\begin{cases} T_\infty &= 205 \text{ K} \\ \rho_\infty &= 4.27\ 10^{-5} \text{ kg/m}^3 \\ Y_{O_2\infty} &= 0.21 \\ Y_{N_2\infty} &= 0.79 \end{cases} \tag{12}$$

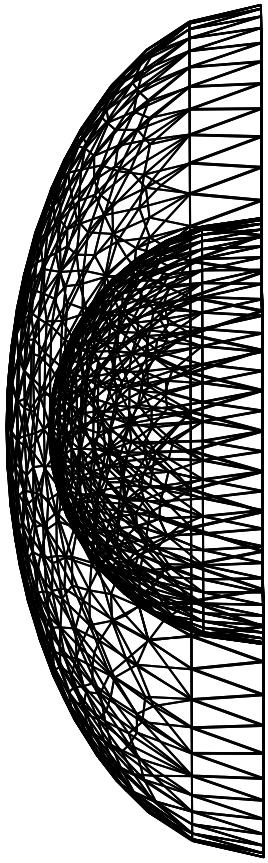

Figure 1: Sphere mesh - 12787 points

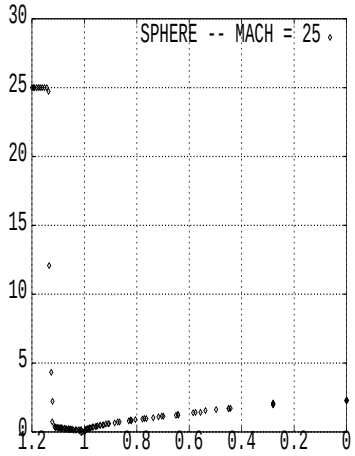

(a) Computational solution; Mach number along the stagnation-point streamline

(b) Theoretical solution; Mach-number isolines

Figure 2: Comparison of the stand-off distance of the shock between the computational solution and the theoretical solution.

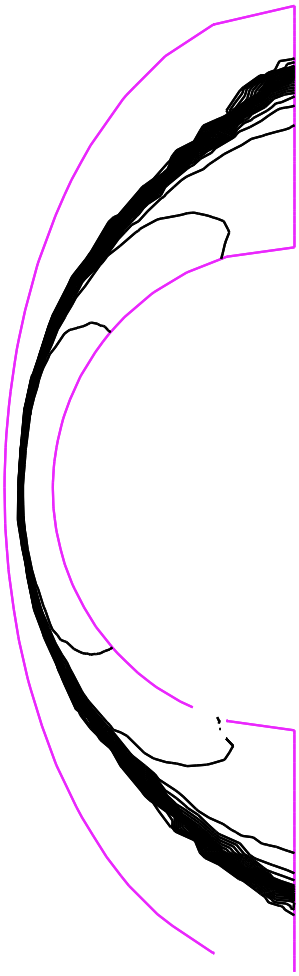

Figure 3: Comparison between the Mach-number isolines of the computational solution and the Mach-number isolines of the theoretical solution

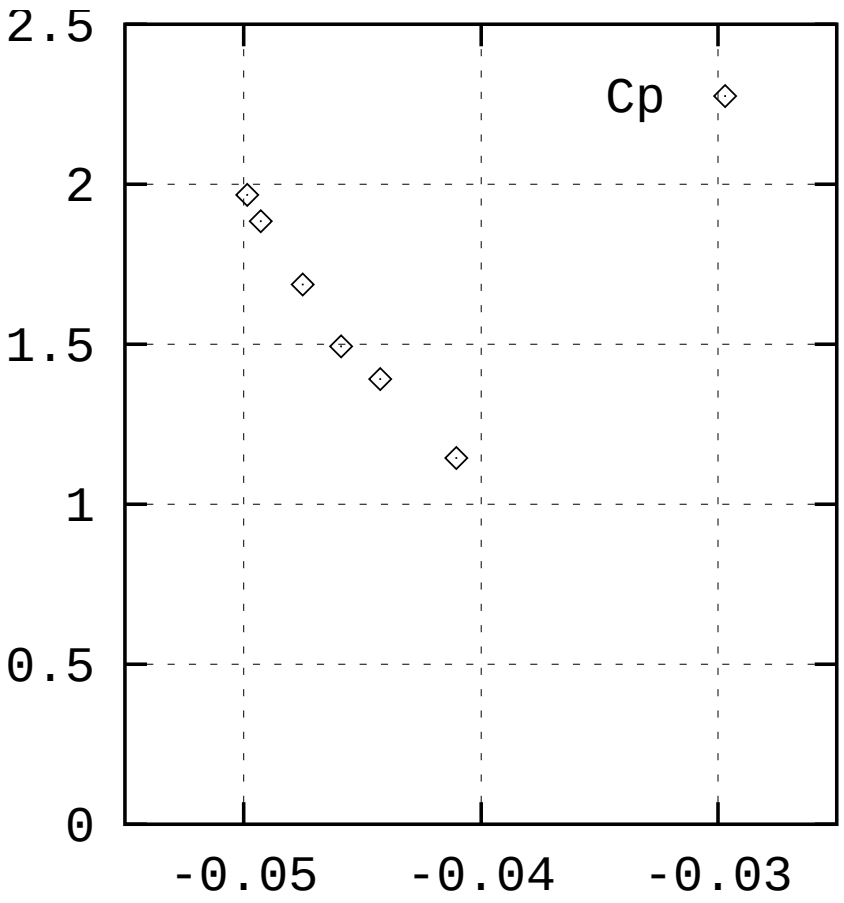

Figure 4: Comparison between the computational solution and experimental results; Sphere – M=12.7; Cp distribution on the body

	kt	CPU time (s)	time per iteration (s)
explicit scheme	8925	16236	1.8
implicit scheme	420	2260	5.4

Table 1: Sphere fisrt-order calculation; Number of time iterations and CPU time needed by both explicit and implicit schemes

and the freestream Mach number $M_\infty = 25$.

The mesh of 12787 points represented on Figure 1 is employed. We represent on Figure 6 the Mach-number isolines. The shock is well captured, the isolines are smooth. The isotherms of the solution are plotted on Figure 7. The temperature in the shock reaches 13596 K and decreases to 9365 K at the stagnation point. On Figure 8 we can see the nitrogen mass fraction isolines of the solution. The nitrogen mass fraction increases from 0. to 0.332 at the stagnation point. We also compute an explicit calculation for this test-case in order to evaluate the efficiency of the implicit scheme. The convergence histories of both explicit and implicit schemes are plotted on Figure 5. The number of time iterations (kt), the CPU time needed to perform the two calculations and the cost per iteration for both schemes are written in Table 1. The explicit scheme needs twenty-one times more time iterations. Of course an implicit time iteration is three times more expensive than an explicit one, but nevertheless the implicit scheme is more efficient than the explicit one by a factor of approximatively seven. We did not succeed to perform a second-order calculation on this mesh, and we decided to use a coarser mesh which has the same number of points than the initial mesh but with the outer boundary further from the body. Of course the shock is not so well captured as in previous calculation. The isolines and the distribution along the stagnation-point streamline of the temperature are plotted respectively on Figure 11 and on Figure 12. On this mesh the temperature reaches 12967 K in the shock. And the nitrogen mass fraction, which is represented on Figure 13, reaches 0.322 at the stagnation point. The convergence of the implicit scheme is of course faster compared with the convergence obtained on the finest mesh, as we can see on Table 2.

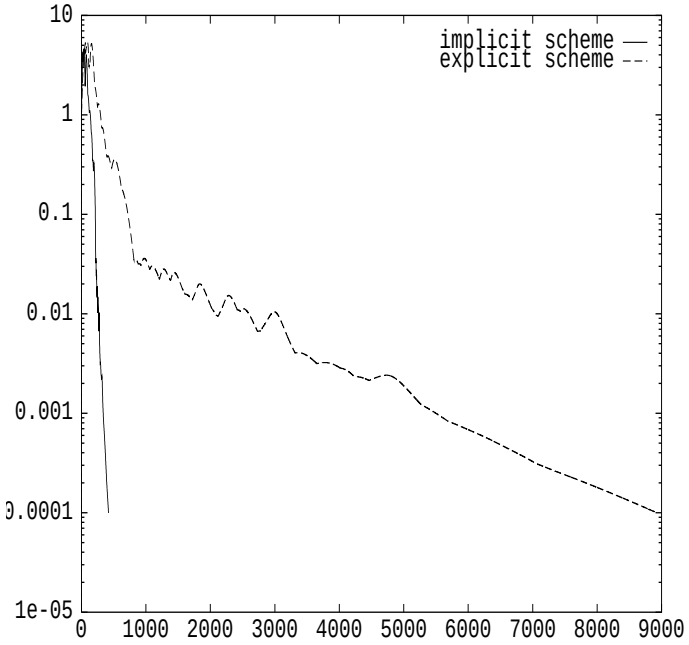

Figure 5: Comparison of convergence histories; explicit scheme vs implicit scheme

	kt	CPU time (s)
implicit scheme	227	1299

Table 2: Sphere first-order calculation; Number of time iterations and CPU time needed by the implicit scheme

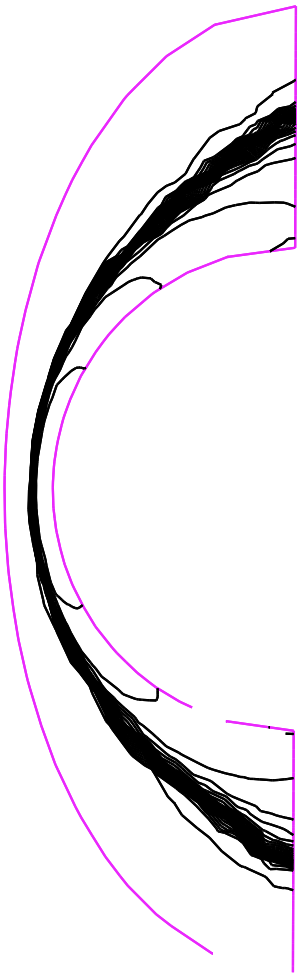

M min $= 0.$ – M max $= 25.$ – $\Delta M = 1.$

Figure 6: Non-equilibrium flow around a sphere – $M_\infty = 25.$; Mach-number isolines

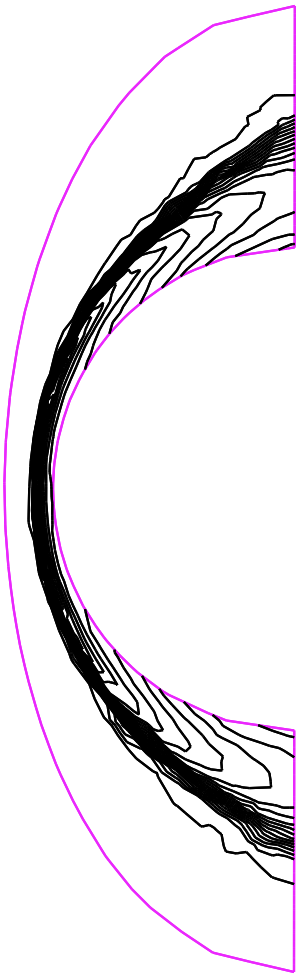

T min = 205. – T max = 13705. – ΔT = 500.

Figure 7: Non-equilibrium flow around a sphere – $M_\infty = 25.$; Isotherms

Y_N min = 0. – Y_N max = 0.33 – $\Delta Y_N = 0.01$

Figure 8: Non-equilibrium flow around a sphere – $M_\infty = 25.$; Nitrogen mass fraction isolines

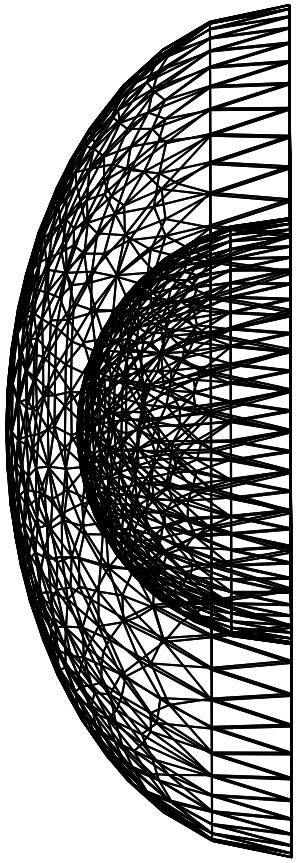

Figure 9: Sphere mesh - 12787 points

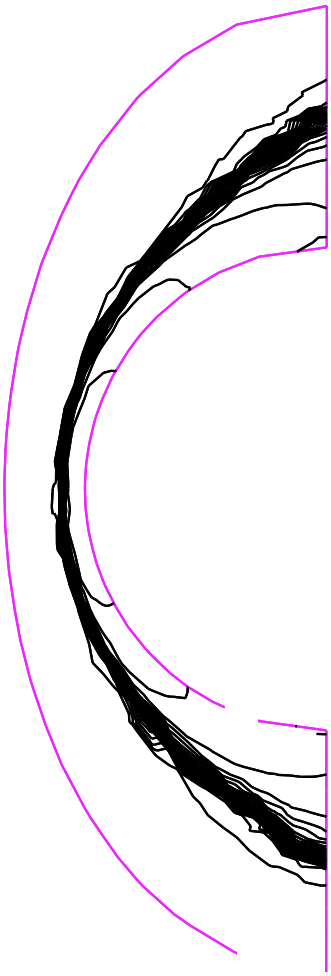

M min $= 0.$ – M max $= 25.$ – $\Delta M = 1.$

Figure 10: Non-equilibrium flow around a sphere – $M_\infty = 25.$; Mach-number isolines

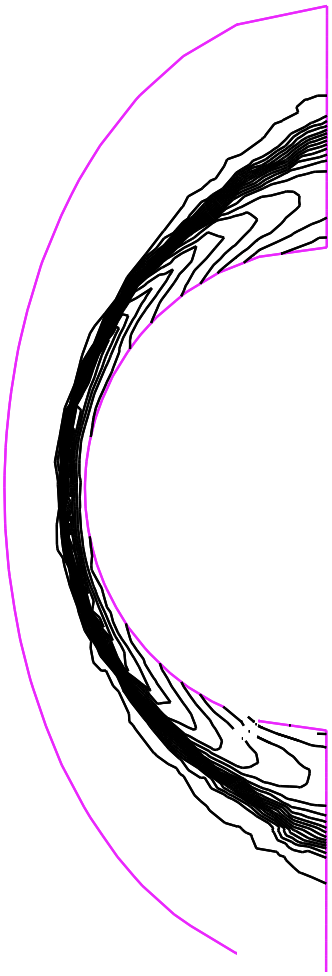

T min $= 205.$ – T max $= 12705.$ – $\Delta T = 500.$

Figure 11: Non-equilibrium flow around a sphere – $M_\infty = 25.$; Isotherms

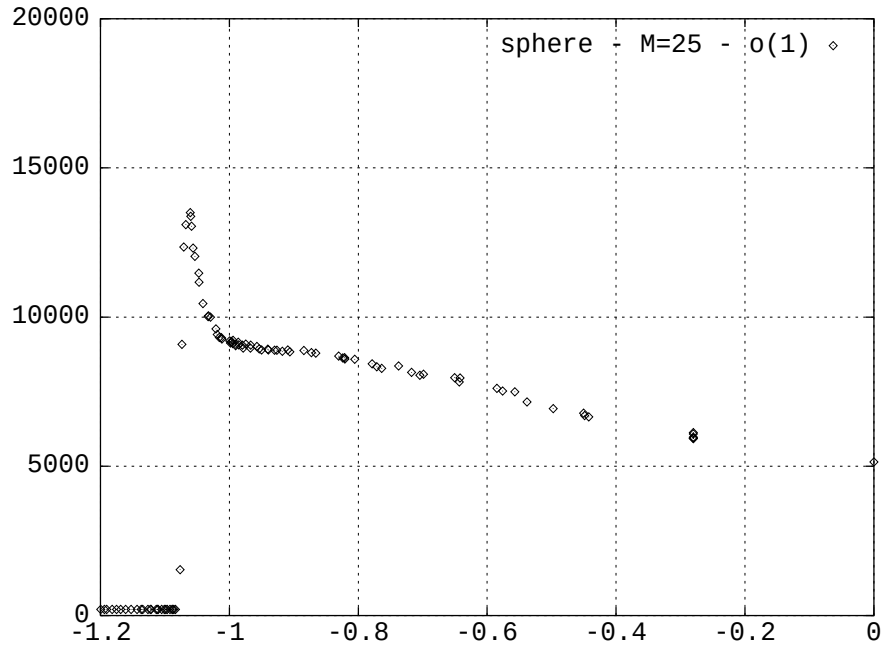

Figure 12: Non-equilibrium flow around a sphere – $M_\infty = 25.$; Temperature distribution along the stagnation-point streamline

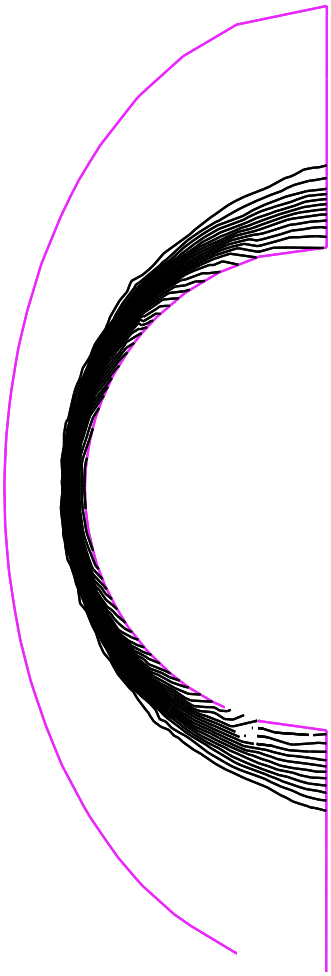

Y_N min = 0. – Y_N max = 0.32 – ΔY_N = 0.01

Figure 13: Non-equilibrium flow around a sphere – $M_\infty = 25.$; Nitrogen mass fraction isolines

Jacobians	kt	CPU time (s)	time per iteration (s)
Van Leer	227	1299	5.7
Steger-Warming	226	1353	6

Table 3: Sphere first-order calculation; Number of time iterations and CPU time needed by the implicit scheme for both sets of Jacobian matrices

4.3.1 Comparison of Jacobians

All the previous calculations were made with the Van Leer for the chemistry scheme (Equ. (10)). The comparison between the two sets of matrices used for the chemistry implicit scheme is made on the coarsest mesh (Figure 9). The two convergence histories obtained with the two sets of matrices (Equ. (10) and Equ. (11)) are plotted on Figure 14 for a maximum CFL number of 20. We find no difference in the convergence histories, but the CPU of the two calculations differ, as we can see on Table 3. The chemistry implicit scheme is somewhat more expensive with the Steger-Warming matrices than with the Van Leer matrices. The comparison of the convergence histories is also made for a maximum CFL number of 25 on Figure 15. The calculation made with the Steger-Warming matrices requires less time iterations than this made with the Van Leer matrices but the oscillations begin at the same iteration for both calculations. In conclusion, the implicit scheme is more economical when using the Van Leer matrices for the chemistry part.

4.3.2 Second-order calculation

A calculation using a second-order spatial approximation has been performed on the previous 12787 points mesh (Figure 9). The initialization is made with the first-order solution. The number of time iterations and the CPU needed for this calculation are reported in Table 4. A second-order time iteration is about 20% more expensive than a first-order one and a second-order calculation needs twice more CPU time than a first-order one. The convergence histories of both first-order and second-order calculations are plotted on Figure 16. We compare the Mach number distributions for both first-order and second-order schemes on Figure 20 and the temperature distributions on Figure 21. We observe that the shock is somewhat closer to the body for the second-

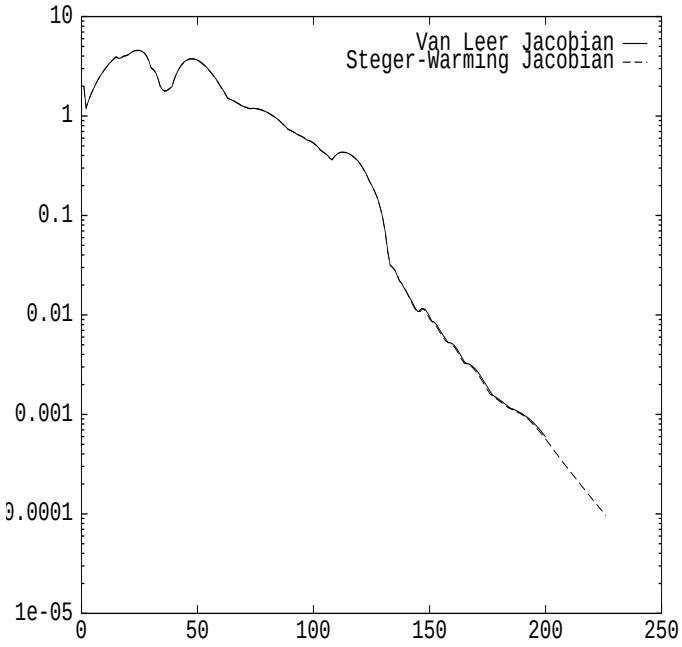

Figure 14: Comparison of the convergence histories for two different sets of Jacobian matrices – $\mathrm{CFL}_{\max} = 20$; Number of time iterations vs residual logarithm

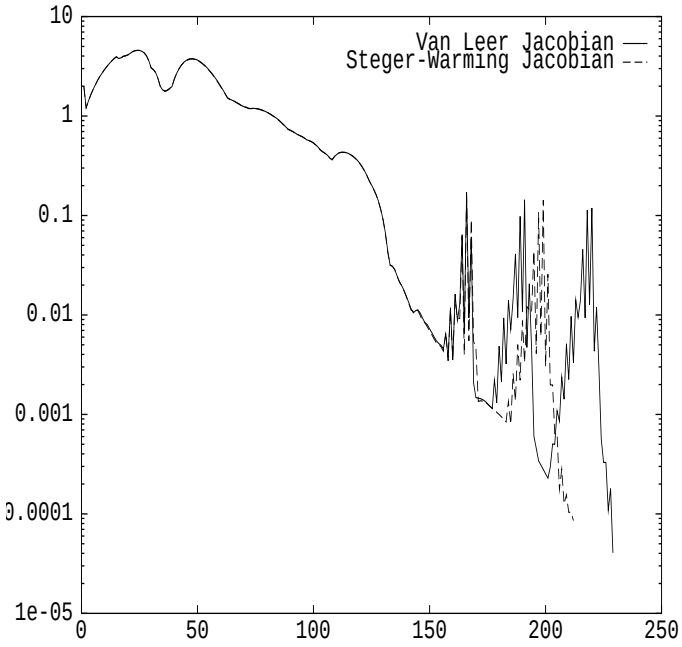

Figure 15: Comparison of the convergence histories for two different sets of Jacobian matrices – $\mathrm{CFL}_{\max} = 25$; Number of time iterations vs residual logarithm

	kt	CPU time (s)	time per iteration (s)
first-order calculation	227	1299	5.7
second-order calculation	288	2060	7.1

Table 4: Sphere calculations; Number of time iterations and CPU time needed by both first-order and second-order schemes

order calculation. The second-order calculation is somewhat more accurate, for example the temperature in the shock reaches 13245 K (instead of 12967 K for the first-order calculation) and the nitrogen mass fraction at the stagnation point reaches 0.334 (instead of 0.322). In conclusion, the second-order scheme is of course more accurate but also more expensive than the first-order one. And for this test-case, for example, it seems more effective to compute a solution using the first-order scheme on a finer mesh (not necessarly with more points but better adapted) than using the second-order scheme on the previous mesh.

4.4 Double-ellipsoid calculations

To illustrate the method, the inviscid flow in chemical non-equilibrium around a double-ellipsoid geometry has been computed. The freestream conditions are those of the standard atmosphere at the altitude of 75 km (12); the freestream Mach number is 25, the angle of attack 30^o. The calculation is made on the 43160 points mesh represented on Figure 22, it is a half mesh cut at the symmetry plane. We use for this computation the second-order implicit scheme. The isolines of the Mach number in the symmetry plane are plotted on Figure 23. We observe a good resolution of the main strong shock and secondary canopy shock which exhibits a small detachment. The isotherms in the symmetry plane are represented on Figure 24. The temperature in the shock reaches 17579 K. We show on Figure 25 and Figure 26 the isolines of the oxygen mass fraction and those of the nitrogen mass fraction respectively . We observe the dissociation of N_2 begins after that of O_2. The dissociation of O_2 is complete while that of N_2 is only partial, the maximum mass fraction of N being equal to 0.3. This solution compares well with computational data existing on the recently installed European Hypersonic Data Base (EHDB) [7].

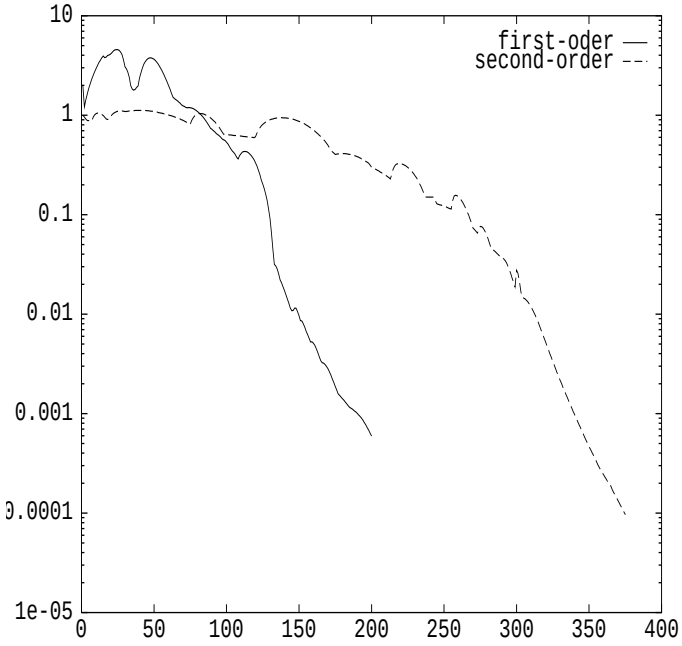

Figure 16: Convergence histories for first-order and second-order spatial approximations; Number of time iterations vs residual logarithm

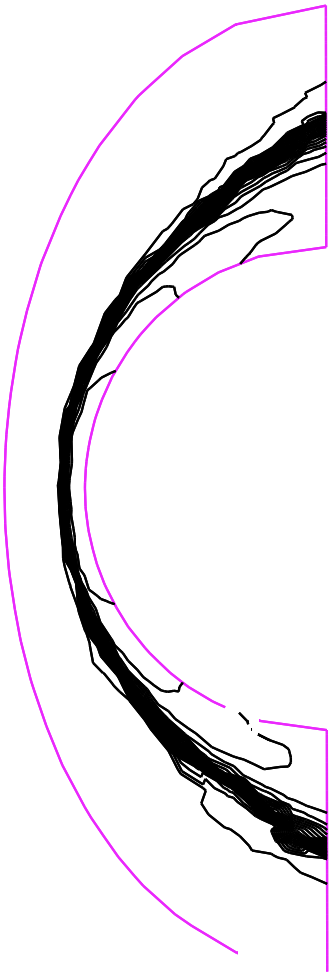

M min $= 0.$ – M max $= 25.$ – $\Delta M = 1.$

Figure 17: Non-equilibrium flow around a sphere – $M_\infty = 25.$; Second-order calculation; Mach-number isolines

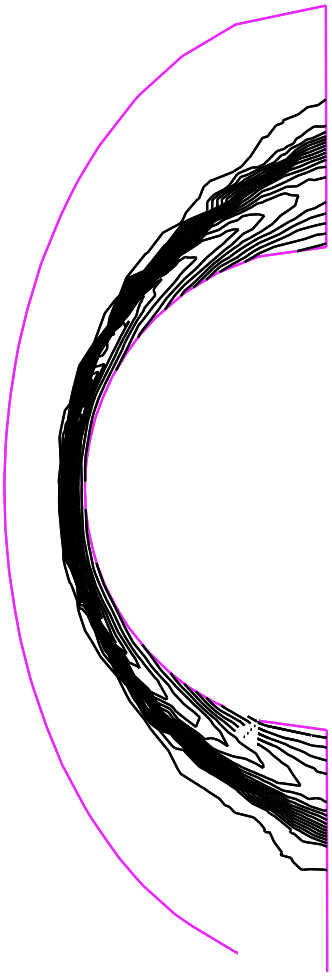

T min = 205. – T max = 13205. – ΔT = 500.

Figure 18: Non-equilibrium flow around a sphere – $M_\infty = 25.$; Second-order calculation; Isotherms

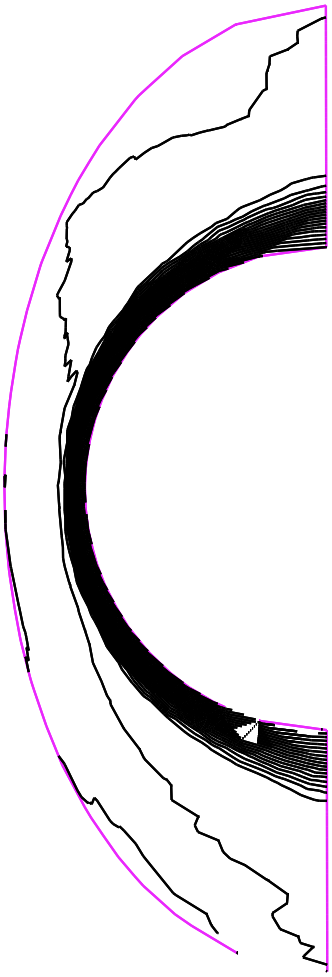

Y_N min = 0. – Y_N max = 0.33 – ΔY_N = 0.01

Figure 19: Non-equilibrium flow around a sphere – $M_\infty = 25.$; Second-order calculation; Nitrogen mass fraction isolines

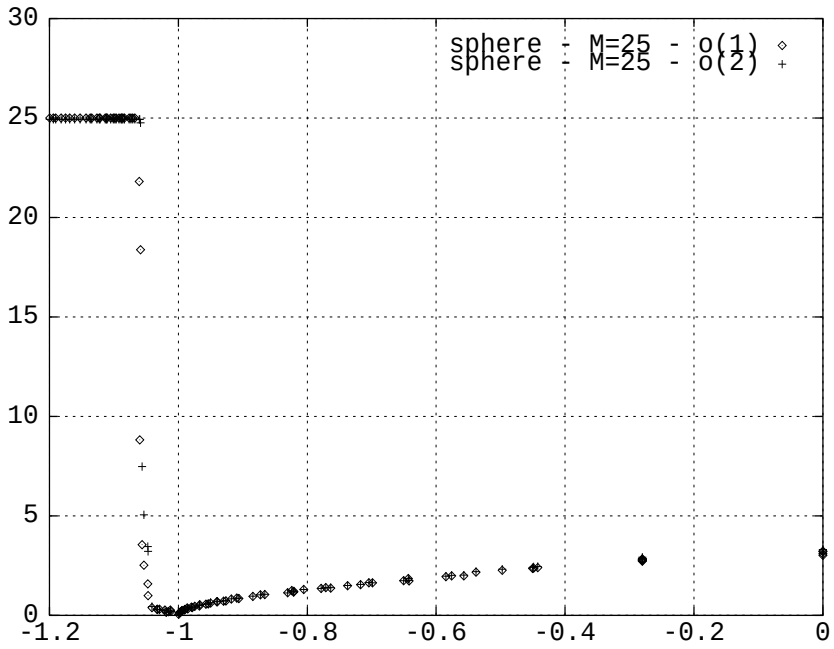

Figure 20: Non-equilibrium flow around a sphere – $M_\infty = 25.$; Mach number distribution along the stagnation-point streamline; First-order/second-order comparison

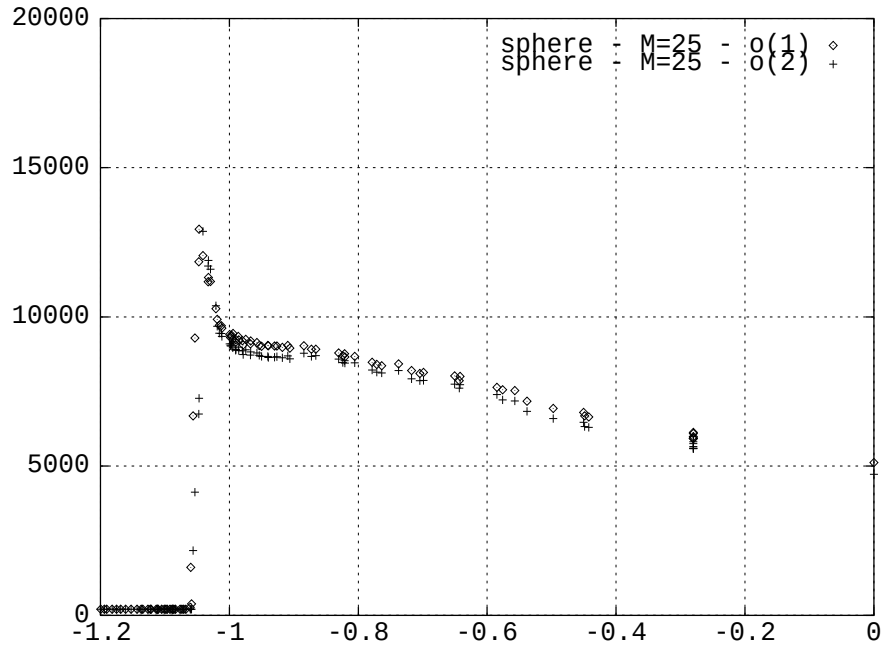

Figure 21: Non-equilibrium flow around a sphere – $M_\infty = 25.$; Temperature distribution along the stagnation-point streamline; First-order/second-order comparison

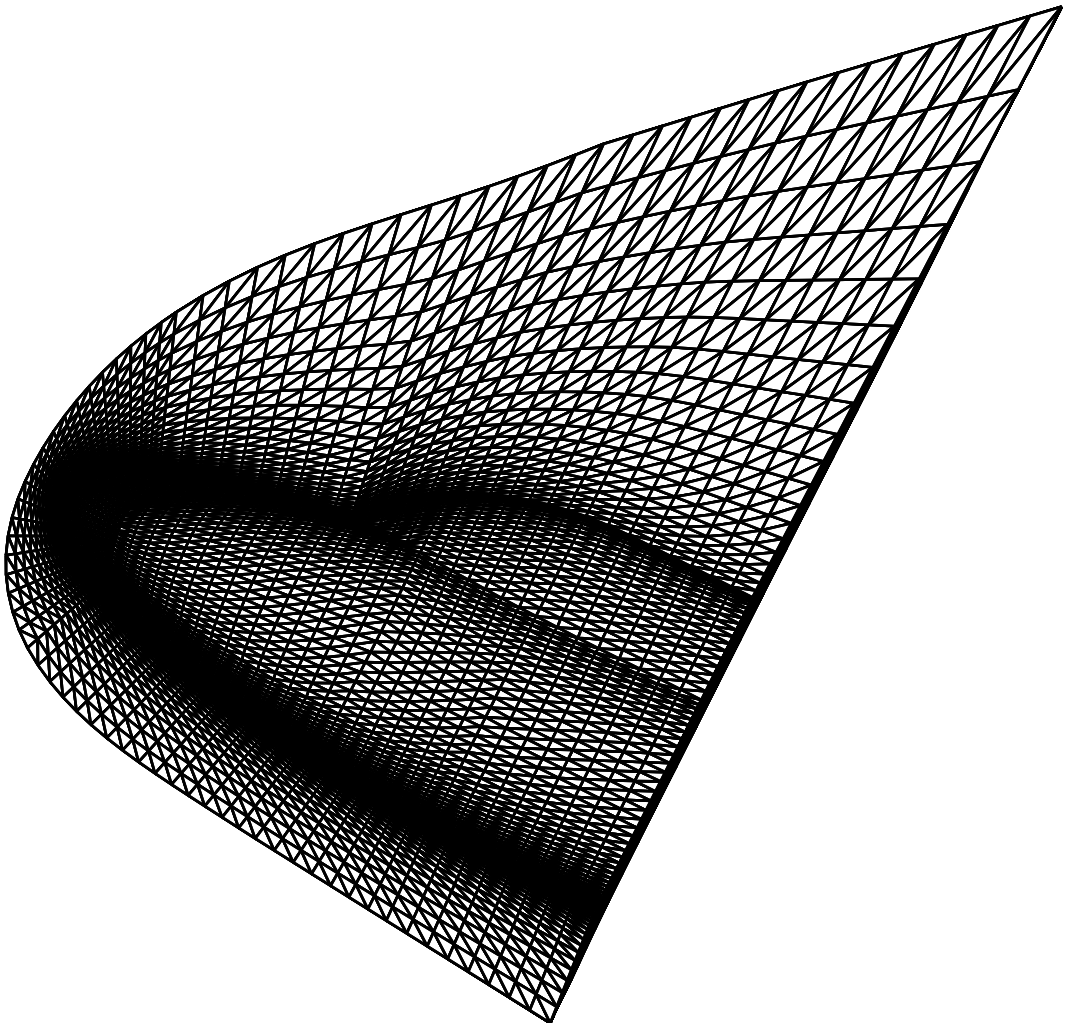

Figure 22: Double ellipsoid mesh; 43160 points

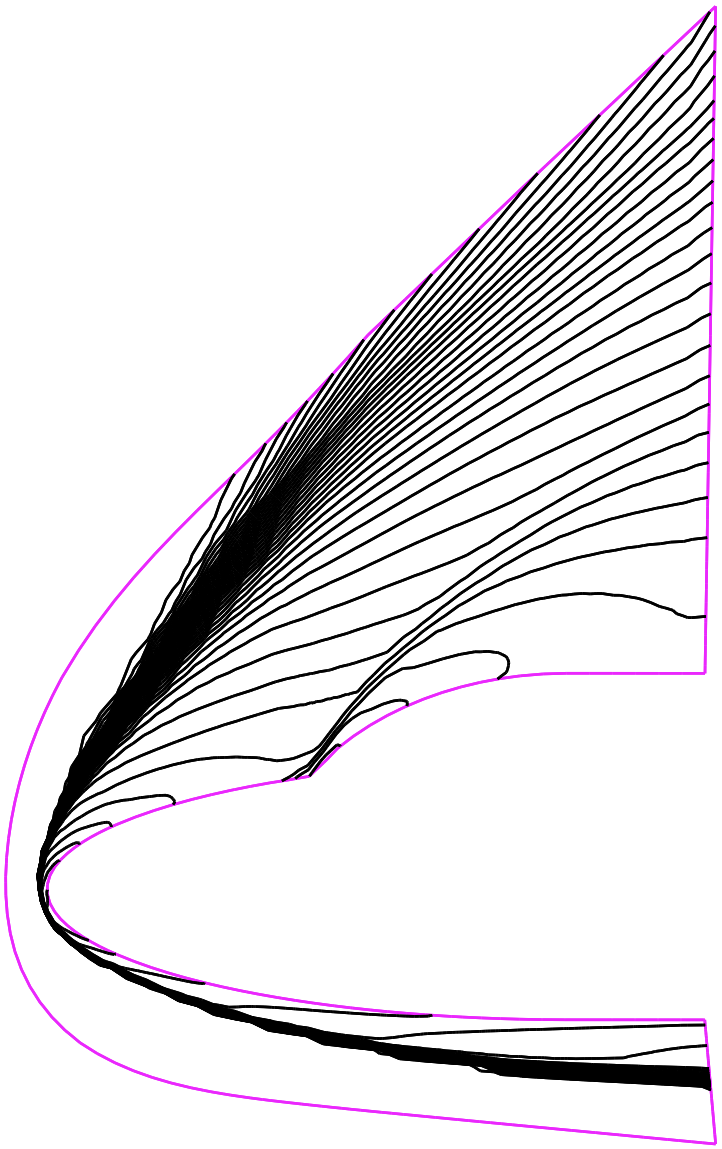

Figure 23: Double ellipsoid calculation; Mach number isolines

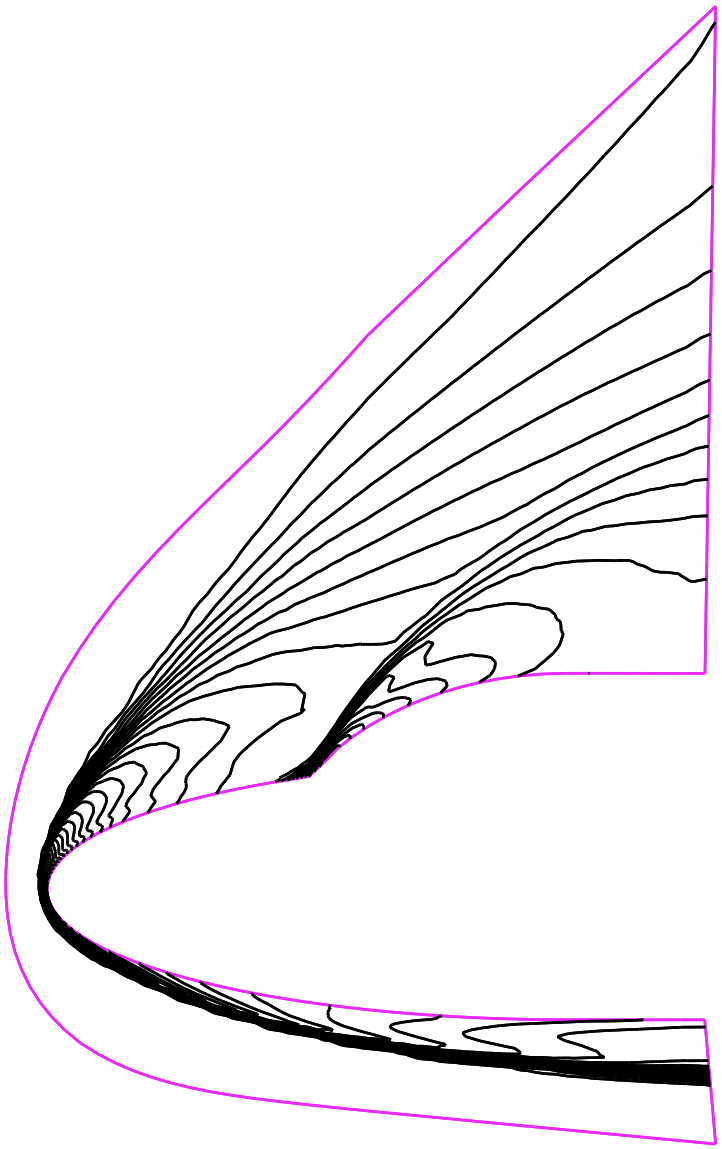

Figure 24: Double ellipsoid calculation; Isotherms

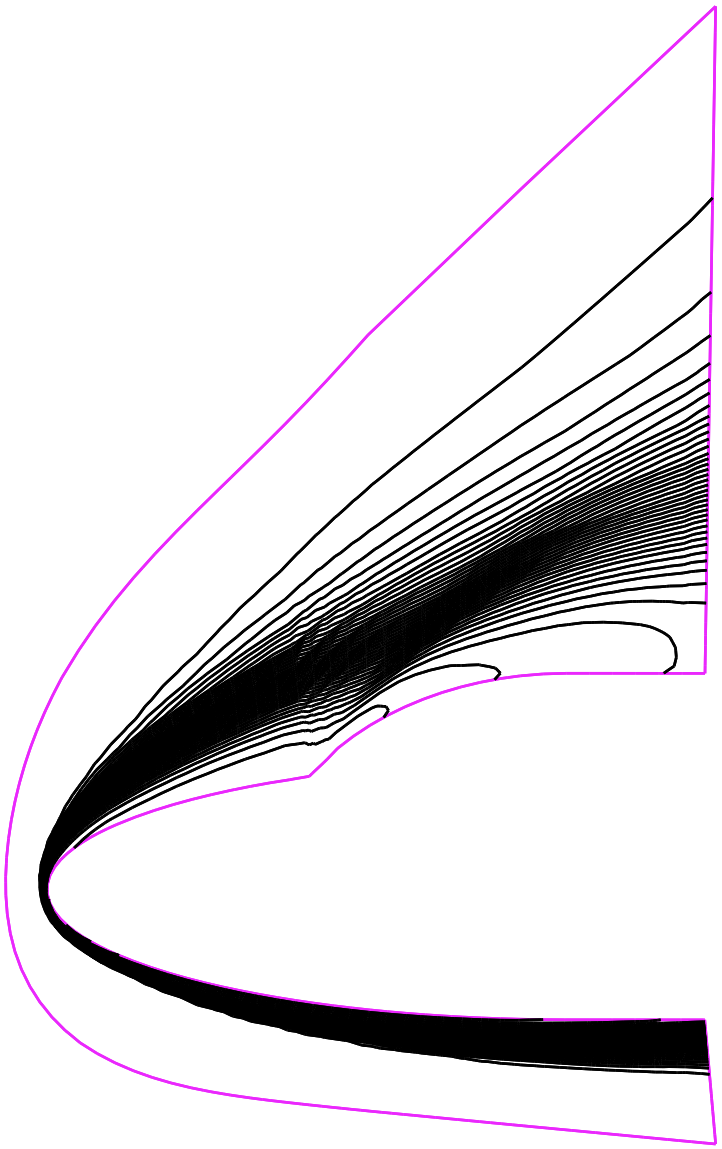

Figure 25: Double ellipsoid calculation; Oxygen mass fraction isolines

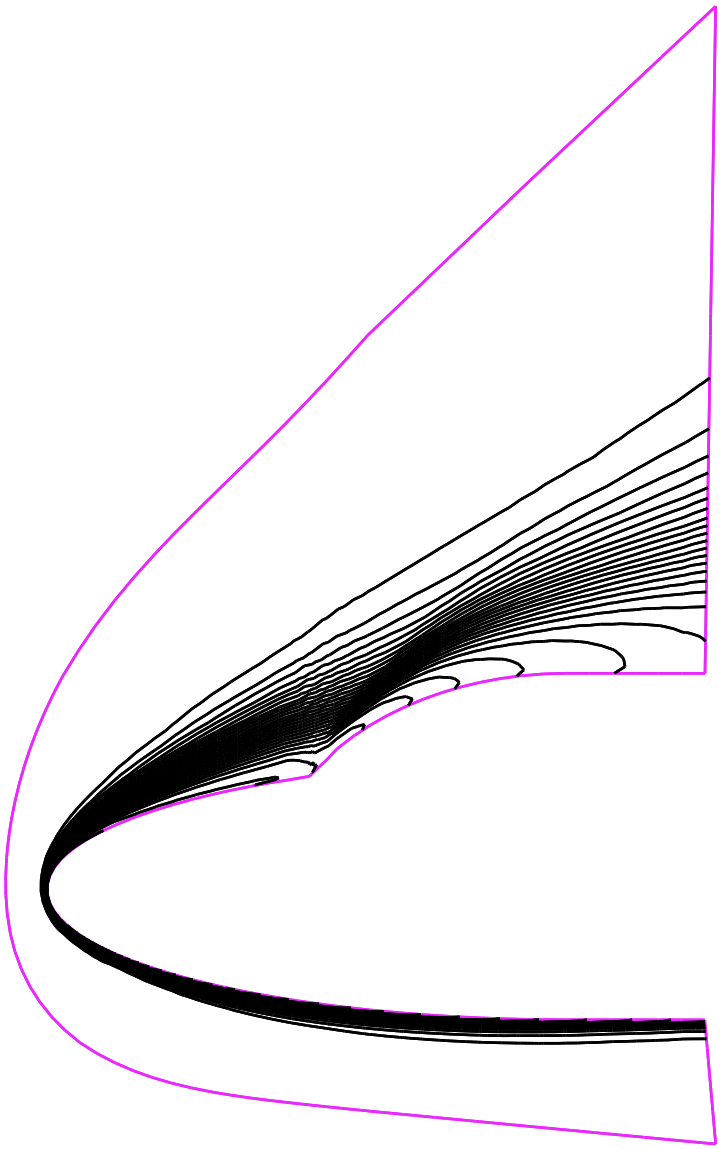

Figure 26: Double ellipsoid calculation; Nitrogen mass fraction isolines

5 CONCLUSION

Two versions of an implicit scheme which differ by the Jacobian matrices have been constructed in both cases of first-order and second-order spatial approximations, for the solutions of 3D hypersonic inviscid flowfields in chemical non-equilibrium.

Several calculations have been made of flows around a sphere of inert and non-equilibrium gas and for different freestream conditions. For all these calculations the implicit scheme is found robust and efficient.

In particular, we have shown that the solution obtained around the sphere compares well with the theoretical one with respect to shock stand-off distances. The C_p distribution of the computed inert-gas solution has been compared with the experimental distribution obtained by Vetter et al. and the results agree well.

We have also been successful in computing the flowfield around a double ellipsoid geometry using a second-order scheme, for a non-equilibrium gas with a freestream Mach-number of 25. This geometry models the nose of a shuttle and has been used for the test-cases proposed in the "Workshop on Hypersonic Flows for Reentry Problems".

In conclusion, the comparison of the numerical results with theoretical, experimental and other computational solutions contributes to the validation of the methodology.

References

[1] *Hypersonic Flows for Reentry Problems, I & II, Springer Verlag, 1991, and III, Springer Verlag, 1992.*

[2] Désidéri, J.-A. and Salvetti, M.V., "Inviscid non-equilibrium flow in the vicinity of a stagnation point", *Comptes Rendus Acad. Sci. Paris, t. 316, Série I, p. 525-530 (1993).*

[3] Park C., "Non-equilibrium Hypersonic Aerothermodynamics", *John Wiley & Sons Inc., 1989.*

[4] Fezoui, L. and Stoufflet, B., "A class of implicit upwind schemes foe Euler simulations with unstructured meshes", *J. Comp. Phys.* **84** *(1), 174-206 (1989).*

[5] Ciccoli, M.C., Fezoui, L. and Désidéri, J.-A., "Efficient Methods for Inviscid Non-equilibrium Hypersonic Flowfields", *La Recherche Aérospatiale* **1**, *p. 37-52 (1992).*

[6] Glinsky, N., Fezoui, L., Ciccoli, M.C. and Désidéri, J.-A., "Non-equilibrium hypersonic flow computations by implicit second-order upwind finite elements", *Proc. Eighth GAMM Conference on Numerical Methods in Fluid Mechanics, Vieweg (1990).*

[7] Abgrall, R., Désidéri, J.-A., Mallet, M., Périaux, J., Perrier, P. and Stoufflet, B., "The European Hypersonic Data Base : a new CFD validation tool for the design of space vehicles", *24th IAAA Fluid Dynamics Conference, Orlando, July 1993, AIAA Paper No. 93-3045.*

[8] Hayes W. D., Probstein R. F., *Hypersonic Flow Theory, vol. I, Applied Mathematics and Mechanics, Academic Press, 1966.*

[9] Vetter M., Olivier H., Grönig H., "Flow over double ellipsoid and sphere - Experimental results", *in [1], III, p. 489-500.*

Unité de recherche INRIA Lorraine, Technôpole de Nancy-Brabois, Campus scientifique,
615 rue de Jardin Botanique, BP 101, 54600 VILLERS LÈS NANCY
Unité de recherche INRIA Rennes, IRISA, Campus universitaire de Beaulieu, 35042 RENNES Cedex
Unité de recherche INRIA Rhône-Alpes, 46 avenue Félix Viallet, 38031 GRENOBLE Cedex 1
Unité de recherche INRIA Rocquencourt, Domaine de Voluceau, Rocquencourt, BP 105, 78153 LE CHESNAY Cedex
Unité de recherche INRIA Sophia-Antipolis, 2004 route des Lucioles, BP 93, 06902 SOPHIA-ANTIPOLIS Cedex

Éditeur
INRIA, Domaine de Voluceau, Rocquencourt, BP 105, 78153 LE CHESNAY Cedex (France)
ISSN 0249-6399